Fachtagung „Experimentelle Strömungsmechanik“
5.-7. September 2017, Karlsruhe

Boundary Layer Characterization during Impulsive Spin-up and Spin-down Motions of High-Reynolds Number Rotating Flow

Grenzschichtcharakterisierung während schneller Spin-up und Spin-down Vorgänge in rotierenden Strömungen bei großen Reynoldszahlen

M. von der Burg[1], **F. Kaiser**[1], **D. Gatti**[1], **B. Schmidt**[1], **J. Sommeria**[2], **S. Viboud**[2], **D.E. Rival**[3] **and J. Kriegseis**[1]

[1] Institute of Fluid Mechanics (ISTM), Karlsruhe Institute of Technology (KIT), Karlsruhe, Germany

[2] LEGI, CNRS UMR5519, University of Grenoble Alpes, Grenoble, France

[3] Department of Mechanical and Materials Engineering, Queen's University, Kingston, Canada

Abstract

Various planar and stereo PIV measurements have been conducted for high-Re in a rotating tank during spin-up and spin-down with the purpose to characterize the side-wall boundary-layer development and corresponding vorticity distributions. The effect of Ekman pumping was successfully suppressed with an additional salt-water layer. An algorithm was developed to identify distinct patterns such as Görtler vortices and transition. Despite a linearly stable character, the spin-up showed transition turbulent for high Reynolds numbers. It is hypothesized that shear-layer instabilities trigger the transition process for high velocities combined with extremely small wall curvature.

Motivation

The interaction of any vortical structure with a wall parallel to its own axis of rotation leads to the formation of a boundary layer with unique features. The wall fed vorticity in the boundary layer is opposed to the vorticity of the initial vortical structure. Consequently, the growth of the boundary layer is driven by vorticity annihilation and the preexisting vorticity in the outer flow (the vortex) influences the momentum transport significantly. Examples can be found in in-flight applications such as strong recirculation zones and leading edge vortices. Buchner et al. [4] recently discussed the influences of vorticity annihilation during the leading edge vortex formation for transitional Reynolds numbers $Re_{\mathrm{chord}} = 10^3 - 10^4$.

A simplified form of the phenomenon was investigated experimentally by Euteneuer [6] and Neitzel & Davis [12]. A tank of radius R, rotating with angular velocity Ω, is spun down to rest from solid body rotation (SBR) with a constant vorticity $\omega_z = 2\Omega$. The flow was investigated in glass cylinders of height H. Large aspect ratios $AR = H/R$ were chosen to ensure small end-wall influence. The opposite signed vorticity in the near wall region fulfills Rayleigh's instability criterion [16] and leads to linear instabilities, which eventually result in streamwise vortices (Görtler-vortices) at the side walls. Their onset and subsequent breakdown due to secondary instabilities was visualized across the circumference by means of aluminium tracer particles for Reynolds numbers $Re = \Omega R^2/\nu < 20{,}000$.

The objective of the present study is twofold. First, the influence of preexisting vorticity in a flow shall be extended towards the turbulent regime and especially towards the following decay of turbulence. This in turn leads to the requirements to expand the Reynolds number of the spin-down experiments by two orders of magnitude. In addition, also the complementary spin-up cases have to be investigated. Even though the spin-up is linearly stable and thus remains laminar for small Reynolds numbers [16], transition to turbulence (thus instability) was observed for the high-Re-range of spin-up. Consequently, spin-up and spin-down cases of similar Reynolds numbers are directly compared.

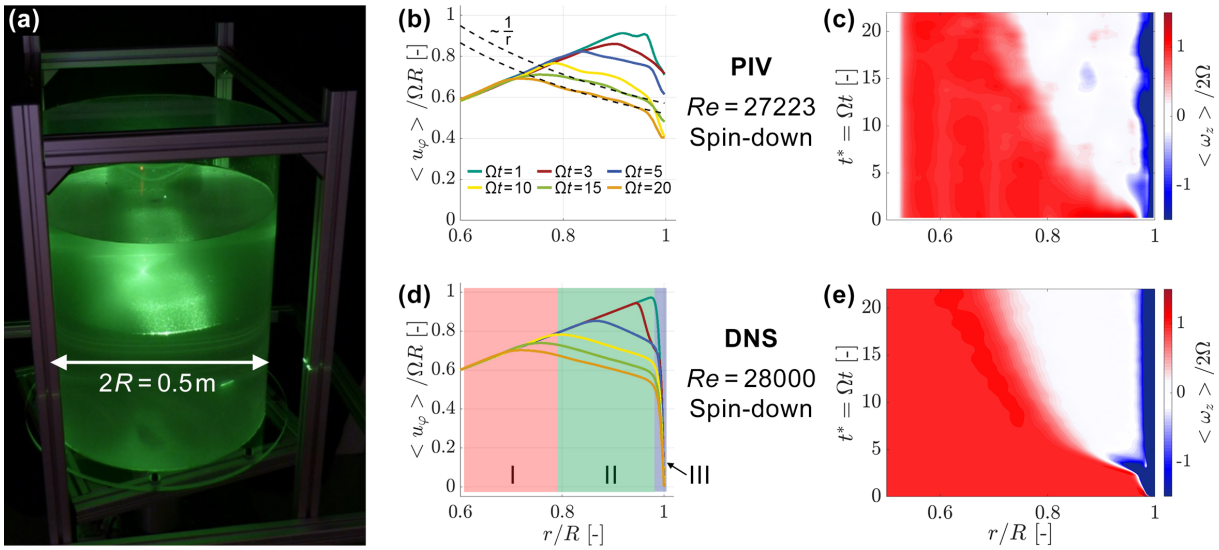

Figure 1: Comparison between DNS and PIV at $Re \approx 28,000$. **(a)** Experimental setup [7], **(b)** measured azimuthal velocity profiles, velocity profiles of potential vortices ($\sim 1/r$, dashed black line), **(c)** measured vorticity development, **(d)** simulated azimuthal velocity profiles, three distinct profile regions for $\Omega t = 10$ (yellow line), **(e)** simulated vorticity development.

The small and moderate Reynolds-number range has already been addressed numerically and experimentally by means of direct numerical simulation (DNS, $Re < 3 \cdot 10^4$) [8] and a tank of $2R = 0.5\text{m}$ diameter (PIV, $Re < 5 \cdot 10^5$) [7]. The results of either study are summarized in Figure 1. After transition to turbulence during spin-down all simulations and experiments reveal the same characteristic behaviour (cp. Figure 1 (b)-(e)). Between the core flow (I) and a shear layer at the outer wall (III) a region of turbulent flow is established, where the spatial average of the axial vorticity $< \omega_z >$ equals zero (II). For the highest simulated Reynolds number of approximately $Re = 28,000$, DNS and PIV results showed good agreement. The white areas of Figure 1 (c,e) depict the quasi irrotational region and the radially inwards growing vorticity annihilation inside the boundary layer. The transition to turbulence occurs at approximately $t^* = \Omega t = 2.5$.

In continuation of the above-reported efforts, the present study covers the high Reynolds-number range $0.5 \cdot 10^6 < Re < 4 \cdot 10^6$. Various planar stereo PIV experiments were conducted at the CORIOLIS platform of the Laboratoire des Écoulements Géophysiques et Industriels (LEGI) in Grenoble, France. This largest rotating platform of its kind is usually applied for experimental modeling of geophysical flows. Additional density stratification or model topography can be installed in this tank [10].

Experimental Procedure

The unique dimensions of this tank ($2R = 13\text{m}$, water level $H \leq 1.2\text{m}$) and $1/\Omega \geq 30\text{s}$ per revolution allowed high spatial and temporal resolutions ($\delta^* = \delta/R$ and $t^* = \Omega t$) for the investigations into the structure and boundary-layer development as required for the present work. The water level was adjusted at $H = 1\text{m}$, which corresponds to an aspect ratio of $AR = 2/13$. The tank acceleration rate ranges around $0.8 - 2.4 \cdot 10^{-6}\text{rad/s}^2$, depending on the chosen offset $\Delta\Omega$ between initial and ultimate angular velocity. Spheroidal powder of polyamide 12 with an average diameter of $30 \pm 2\text{m}$ (Orgasol®2002 ES3 NAT, particle density and relaxation time $\rho_p = 1.03\text{kg/m}^3$ and $\tau_p = 50\text{s}$) was used as tracer particles. These particles are characterized by a very low deviation in diameter and near-neutral buoyancy in water [1]. The remaining differences were further reduced with salt, i.e. the water density was slightly increased to $\rho_f = 1.004\text{kg/m}^3$. This was particularly important in the present case, since several hours were required for the fluid to return to quiescent conditions after particle supply. The Stokes number for the given parameters is $Stk = 0.03$, where the flow relaxation time is determined with the wall-velocity and the characteristic diameter of the Görtler vortices.

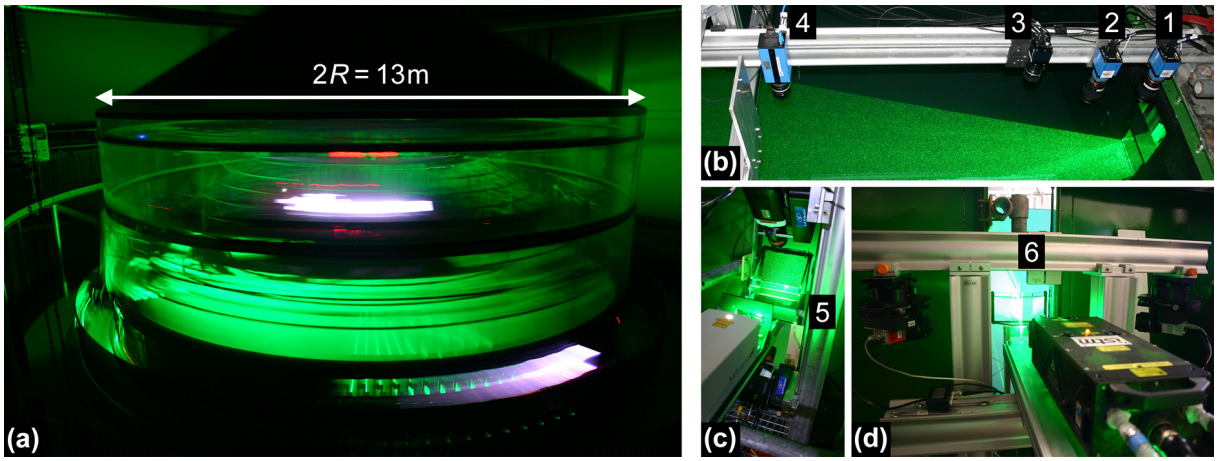

Figure 2: Experimental setup of all PIV experiments as conducted simultaneously in the rotating CORIOLIS tank **(a)**; planar measurements in the $r-\varphi$ plane **(b)**, stereo measurements in the $r-\varphi$ plane **(c)** and the $r-z$ plane **(d)**.

In order to capture different phenomena in the rotating flow simultaneously, three PIV setups were installed, which comprised two laser light sheets and eight cameras. All equipment was placed on the rotating platform, such that the data was obtained in a rotating frame of reference; see Figure 2. A continuous wave laser (25W Spectra Physics Millennia) was introduced through a side window to span a horizontal light sheet at a height of $0.6\mathrm{m}$ ($r-\varphi$ plane). Four cameras were mounted overhead to perform planar PIV through the free surface as indicated in Figure 2 (b).

Two pco.edge 5.5 (Cam1 and Cam2) each equipped with a $35\mathrm{mm}$ lense and aperture of 2.8, and a Dalsa Falcon 4M (Cam3) with a $28\mathrm{mm}$ lense and aperture of 2.8 were operated in global shutter mode at identical frame rate ($25\mathrm{Hz}$-$200\mathrm{Hz}$) to build a wide field of view (FOV) of $75\mathrm{cm}$ in radial direction with approximately $10\mathrm{px/mm}$ spatial resolution. Accordingly, only the azimuthal direction of the sensor was cropped to meet the requirements for the high frame rates. A large particle displacement of approximately $30\mathrm{px}$ was chosen. Due to the tank-fixed reference frame the particle displacement is predominated by azimuthal motion. Both radial and axial displacements are one order of magnitude smaller, i.e. approximately $3\mathrm{px}$. No critical particle loss due to out-of-plane movement was observed.

A fourth camera (pco.1200 HS), was mounted $1.5\mathrm{m}$ inwards from the side wall to quantify changes in the azimuthal velocity profile, which are introduced by end-wall effects like Ekman pumping [5]. Due to its location in large distance from the side wall, any influence of the side wall boundary layer during the measurement time was excluded.

The horizontal light sheet was further used for a stereo PIV setup, where two Phantom Miro M310 cameras (Cams5) recorded images through the side window with an angle of 45° to the light sheet; see Figure 2 (c). This additional setup was added was chosen to investigate the near-wall instability process and the out-of-plane motion early on during boundary-layer development. Nikon AF micro-nikkor 60mm objective lenses ensured a highly resolved near wall region. The frame rate of Cams5 doubled the frame rate of Cams1-4.

A second stereo PIV setup was installed at an additional side wall window to record data in the $r-z$ plane; see Figure 2 (d). The low speed system ($5\mathrm{Hz}$, double frame) comprised two ILA.PIV.Nano cameras (Cams6) equipped with $50\mathrm{mm}$ lenses (aperture 16), and a dual cavity laser (Quantel EverGreen). The FOV size was $7\times 7\mathrm{cm}^2$ with corresponding magnification factor of approximately $13.5\mathrm{px/mm}$. Water filled acrylic prisms and Scheimpflug adapters were used for either stereo setup to minimize distortion issues and adjust the focus plans; see Figure 2 (c,d).

In order to minimize the end-wall effects on the boundary-layer development, Nordsiek et al. [13] recommend the use of density mismatched fluids to confine end wall effects to a dense layer at the bottom. Accordingly, approximately three tons of salt were used to produce an $8\mathrm{cm}$ heavy salt

Name	Reynolds number $\times 10^6$	Delta RPM	repetitions (total)	repetitions (with salt water)
470s Spin-up	0.5	0.1277	1	-
470s Spin-down	0.5	-0.1277	2	-
240s Spin-up	1	0.25	3	1
240s Spin-down	1	-0.25	2	-
120s Spin-up	2	0.5	6	3
120s Spin-down	2	-0.5	8	3
90s Spin-up	2.6	0.6666	2	-
90s Spin-down	2.6	-0.6666	4	2
60s Spin-up	4	1	3	-
60s Spin-up	4	-1	3	-

Table 1: Conducted experiments sorted by Reynolds number.

water layer at the bottom of the tank and was tested for some parameters. All investigated parameter combinations, repetitions with and without salt-water layer are listed in Table 1.

The Reynolds number of the slowest rotational speed of 0.1277 revolutions per minute (RPM) measured in Grenoble was set to match the highest Re of our earlier experiments ($R = 0.25\mathrm{m}$) [7]. The measurement setup was slightly adapted to the requirements of the specific experiment. Since surface waves occurred for rotational speeds $\Delta\Omega \geq 0.66$, Cam1 was moved to the bottom window and equipped with a $20\mathrm{mm}$ lens. The FOV changed from $21 \times 25\mathrm{cm}$ to $40 \times 50\mathrm{cm}$ with spatial resolution of $5.6\mathrm{px/mm}$.

Precise identification of location and orientation in the huge tank required various additional calibration steps for all FOVs beyond the standard calibration target recordings. Particularly, a rope spanned from the center of rotation to the wall served as radial axis. Combined with a ruler for radial displacement from the wall and a dotted grid for identification of the magnification factor, all necessary information for the transformation from pixel space to physical space was available. All snapshots obtained in the horizontal plane were processed with the open-source Matlab toolbox UVMAT [9]. The additional images of the vertical plane were processed with the commercial software PIVview [15].

End-wall effects

Euteneuer [6] stated that an aspect ratio of $AR = 4$ as to be sufficiently high to reduce the bottom wall influence, which was later increased to $AR = 18.7$ by Mathis & Neitzel [11]. Since both values are much higher than the present case of $AR = 2/13$, bottom wall effects like Ekman pumping and corner vortices will increasingly influence the measured flow after a certain time Ωt. Benton & Clark Jr. [2] predicted a very early onset of such flows starting from $\Omega t \approx 1$. Furthermore, O'Donnell and Linden [14] stated that vortex stretching by the motion of the surface adds to the Ekman pumping in the outer region of the tank but hinders spin-up near the axis. Both the effects of Ekman pumping and its suppression with a salty bottom layer [13] are indicated in Figure 3, where the averaged azimuthal velocity u_φ of the Cam4-FOV is plotted over time for both spin-up and spin-down, with and without the heavy salt water layer.

The angular velocity of the spin-down case without the salt water layer decelerates drastically after $\Omega t \approx 3$. Obviously, the use of a salt water layer clearly delays this impact of the bottom wall beyond $\Omega t = 20$ even for such a small aspect ratio. At first glance, the spin-up case seems to remain unaffected with and without salt water layer. However, evaluations of the near wall data show an influence of the bottom wall also in the spin-up case. Therefore, it is hypothesized that the dominant phenomenon in the spin-up case are corner vortices, which are not captured by Cam4. However, a more global phenomenon such as some strongly non-linear Ekman pumping dominates the spin-down case. While the details of the bottom wall effects are still under investigation, the preliminary conclusion is that the introduced salt water layer enlarges the time frame for a mostly undisturbed side-wall boundary layer growth from $t^* = \Omega t \approx 3$ to $t^* = \Omega t > 20$.

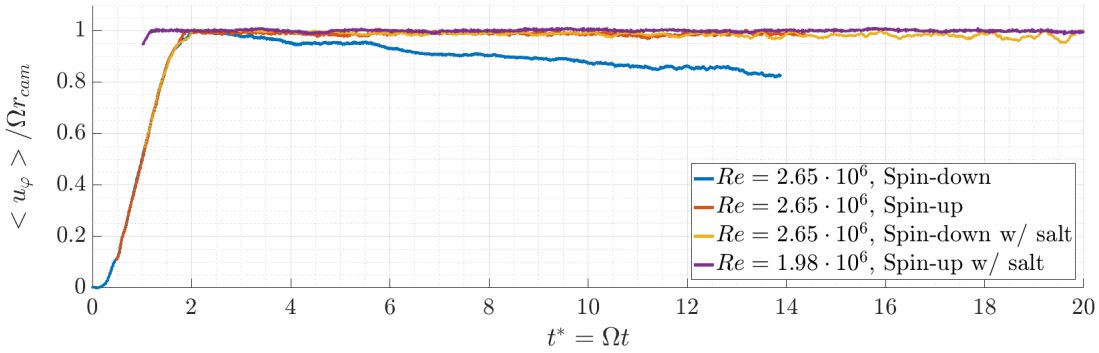

Figure 3: Influence of the bottom wall on the normalized velocity u_φ for spin-up and spin-down cases with and without a heavy salt water layer (Cam4, $r/R = 0.77$).

Transition

For spatially developing boundary layers earlier work showed the existence of Görtler vortices even for really large radii up to 20m [3]. The coherent structures found in our spin-down experiments and complementary DNS agree well with the earlier reports. Therefore, the term *Görtler vortex* (GV) will also be used for the streamwise elongated structures occurring during transition to turbulence as sketched in Figure 4(a). GVs were captured in multiple experiments with the vertical stereo and the horizontal system; see Figure 4(b-e). While the footprint of GVs appears as bands in Cam1 (b,d), the GVs appear as plumes of a smaller out-of-plane component in the vertical stereo FOV of Cams6 (c,e). Since the transition to turbulence occurs before $t^* = 2.5$ for all experiments, the analysis of the transition process and underlying instability mechanism is not limited to the salt water experiments.

The GV-onset time, the time of GV break down as well as an appropriate transition time were identified by means of a custom algorithm based on the azimuthal mean of the axial component of vorticity $< \omega_z >_\varphi(r)$. The algorithm was applied to the data of Cam1. To account for measurement errors of the derived quantity ω_z, the median of its azimuthal standard deviation $\widetilde{\sigma^{\omega_z}_{\varphi}}_r$ is defined as noise floor. This floor is then added and subtracted from the median of the azimuthal mean vorticity $(\widetilde{< \omega_z >_\varphi})_r$ to determine upper and lower threshold levels.

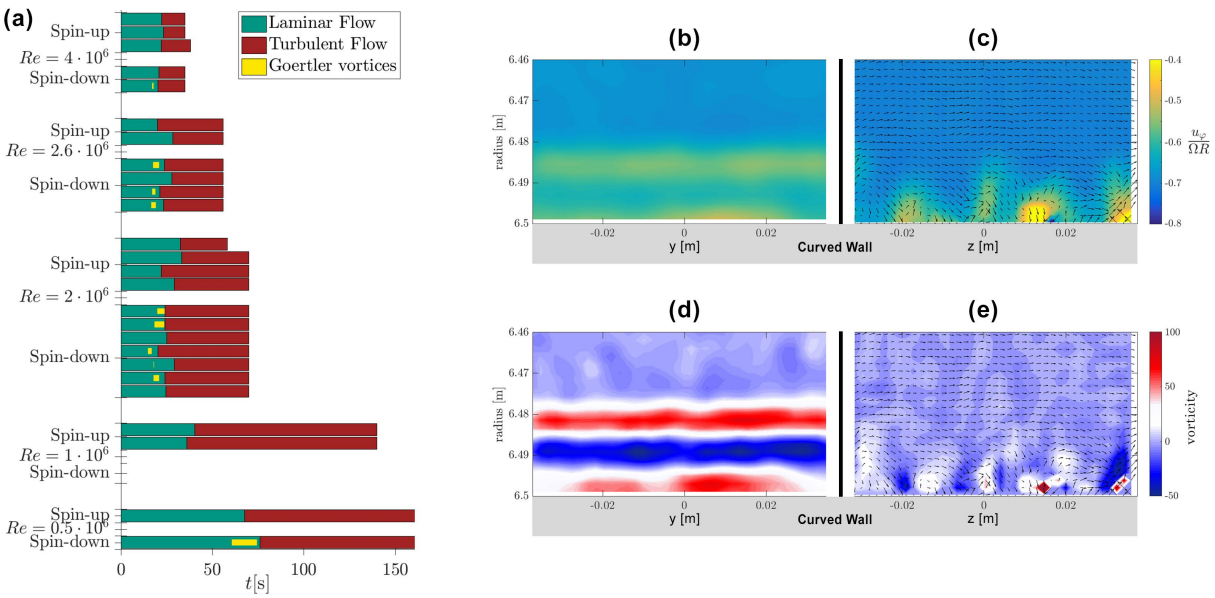

Figure 4: **(a)** Laminar and turbulent flow states as well as identified GVs. Due to different acceleration ramps (between $14 - 24$s) the physical time is displayed; **(b,c)** velocity and **(d,e)** vorticity fields around GVs in the horizontal FOV of Cam1 **(b,d)** and vertical FOV of Cams6 **(c,e)**.

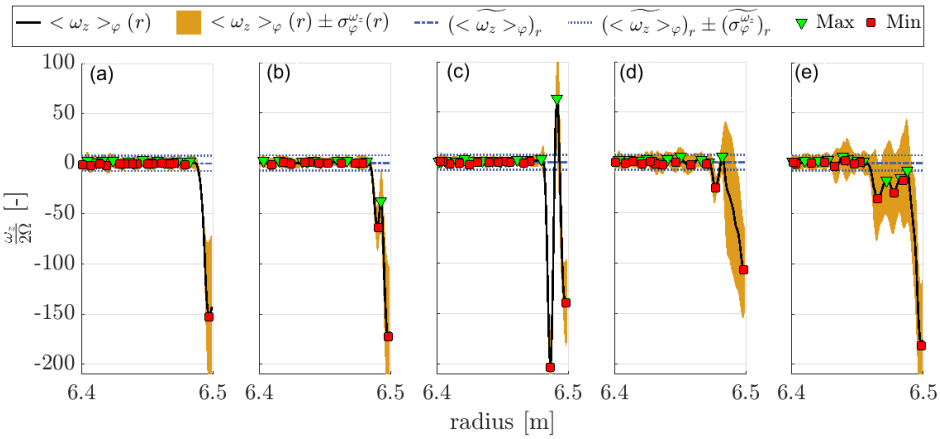

Figure 5: Axial vorticity $\omega_z/2\Omega$ and results of the applied GV-identification algorithm; **(a)** Laminar flow, **(b)** GV-onset, **(c)** GV, **(d)** GV break up, **(e)** turbulence.

The results are shown in Figure 5, where the laminar flow state (a) only reveals a single distinct vorticity peak at the wall. During GV-onset (b), an additional pair of local peaks occurs between wall and the unperturbed flow, which grows towards a fully developed GV (c). The distinct peaks vanish again during break up (d), which coincides with an increasing noise flow (i.e. fluctuations) of the vorticity along circumference. After the transition to turbulence, the curve comprises multiple local peaks below the lower threshold (e).

Note that the diagrams of Figure 4(a) have been derived based on the above-introduced algorithm. Two conclusions can be drawn from this chart: First, for identical Reynolds numbers the transition to turbulence of the spin-up case occurs after the appearance of first instabilities in the corresponding spin-down case. The transition is expedited for higher Reynolds numbers. Second, GVs do not contribute to the instability process during spin-up, even though shear layer instabilities can be seen in the data as illustrated in Figure 6. Obviously, the coherent structures are smaller in size during spin-down, which comes as a result of the initial opposite signed vorticity. A GV is captured for approximately 13.5s during spin-down at $Re = 2 \cdot 10^6$, which corresponds to an azimuthal length of the structure of approximately 1.2m.

The spatio-temporal evolution of the boundary-layer growth and corresponding vorticity formation and annihilation is shown in Figure 7 for a spin-down at $Re = 2 \cdot 10^6$. Three horizontal lines are

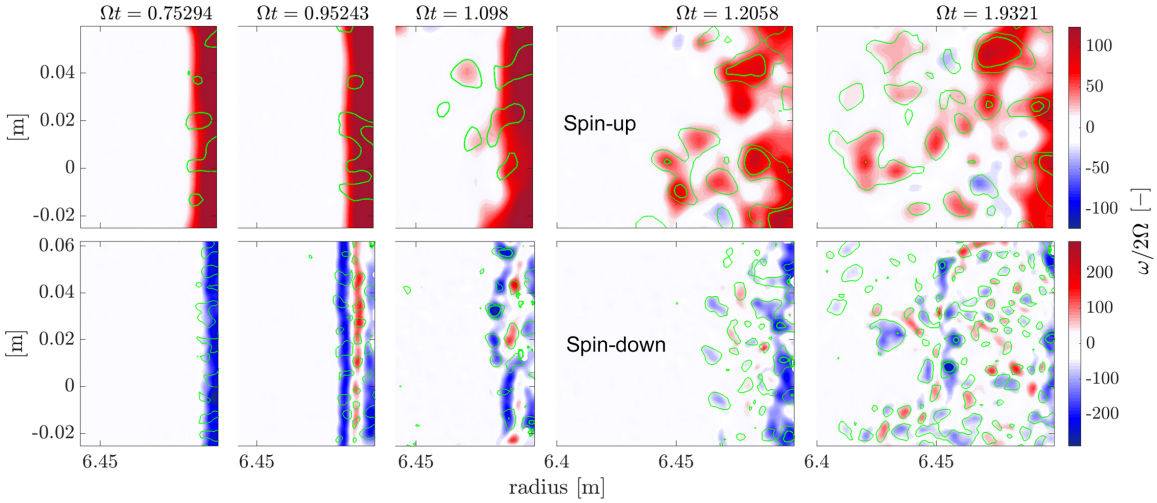

Figure 6: Temporal sequence of the transition to turbulence for spin-up (upper row) and spin-down cases (lower row), $Re = 2 \cdot 10^6$.

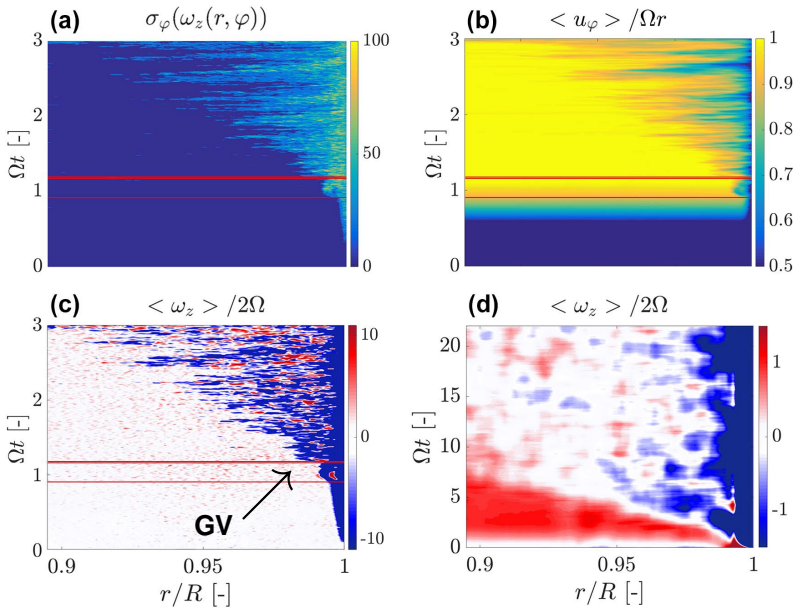

Figure 7: Spatio-temporal boundary-layer development during spin-down at $Re = 2 \cdot 10^6$, instances of GV onset, GV break up and subsequent transition are indicated with red lines (bottom to top); **(a)** azimuthal standard deviation of vorticity, **(b)** spatially averaged azimuthal velocity, **(c)** azimuthally averaged vorticity for spin-down without salt water layer, **(d)** azimuthally averaged vorticity for a spin-down with salt water layer.

added to the diagrams to indicate the instances of GV onset, GV break up and subsequent transition (bottom to top). The azimuthal velocity is plotted in Figure 7(b), which also indicates the duration of the ramp-up process of the spin-down. The corresponding vorticity distribution and its standard deviation are shown in Figures 7(c) and 7(a), respectively. Note that the red vorticity pattern at $t^* \approx 1$ immediately emphasizes the presence of a GV, as illustrated in Figures 4(b) and 6. Similar to the small and moderate Reynolds numbers, the growth rate of the boundary layer instantly increases after GV break up, when the transition to turbulence occurs (cp. Figure 1). The results of a salt-water experiment are added in Figure 7(d) for comparison purposes, which demonstrates the annihilation process, i.e. development of the quasi irrotational region II, more saliently at $t^* > 7$.

Concluding Remarks

Various planar and stereo PIV measurements have been conducted for high-Re in a rotating tank during spin-up and spin-down with the purpose to characterize the boundary-layer development and corresponding vorticity distributions. Due to the large dimensions of the test facility, the obtained data show very high temporal and spatial resolutions on the normalized scales. The introduction of a heavy salt layer at the bottom of the tank significantly delayed the influences of Ekman pumping during both, spin-up and spin-down experiments. This is a valuable insight for experimental research of rotating flows beyond the present study, since an additional heavy layer indeed qualifies low-aspect-ratio tanks to mimic large-aspect-ratio flow scenarios. In the present study (high Re, small AR), the salt layer allowed the analysis of the boundary-layer development on normalized time scales similar to those of the small- and moderate-Re cases and, therefore, allows the analysis beyond the transition to turbulence and towards its decay.

An algorithm was developed with the purpose to characterize relevant flow features during spin-up and spin-down from vorticity fields. This algorithm provides sufficient information on the temporal character of the boundary layer development. As expected, no GVs were found during spin-up. However, it turned out that even during spin-down maneuvers the GV development became weaker with increasing Re, which indicates the competition between inertia and pressure gradients. Interestingly, the high-Re experiments also revealed transition to turbulence even for the spin-up cases, despite a linear stability according to Rayleigh [16]. It is, therefore, hypothesized that shear-layer instabilities

might trigger the transition process for high velocities combined with extremely small wall curvature. However, further investigations will be necessary to test this hypothesis.

The forthcoming steps will revolve around the analysis of the time-resolved stereo data of the $r-\varphi$ plane. Particularly, the analysis of the out-of-plane motions in proximity of the outer wall might provide a deeper insight into the GV development.

Acknowledgements

This work is supported as project ANNI by the European High-Performance Infrastructures in Turbulence Consortium (EuHIT).

References

[1] Arkema. Orgasol®, 2017. URL http://www.orgasolpowders.com/en/product-features-benefits-and-grades/main-properties/.

[2] E.R. Benton and A Clark Jr. Spin up. *Annual Review of Fluid Mechanics*, 6:257–280, 1974.

[3] H. Bippes. Experimentelle Untersuchung des laminar-turbulenten Umschlags an einer parallel angeströmten konkaven Wand. In *Sitzungsberichte der Heidelberger Akademie der Wissenschaften*, pages 103–180. Springer-Verlag, 1972.

[4] A.-J. Buchner, D. Honnery, and J. Soria. Stability and three-dimensional evolution of a transitional dynamic stall vortex. *Journal of Fluid Mechanics*, 823:166–197, 2017.

[5] P. W. Duck and M. R. Foster. Spin-up of homogeneous and stratified fluids. *Annual review of fluid mechanics*, 33(1):231–263, 2001.

[6] G. A. Euteneuer. Die Entwicklung von Längswirbeln in zeitlich anwachsenden Grenzschichten an konkaven Wänden. *Acta Mechanica*, 3(13):215–223, 1972.

[7] F. Kaiser, T. Wahl, D. Gatti, D.E. Rival, and J. Kriegseis. Vorticity propagation for spin-up and spin-down in a rotating tank. *18th International Symposium on the Application of Laser and Imaging Techniques to Fluid Mechanics, Lisbon, Portugal*, 2016.

[8] F. Kaiser, D. Gatti, B. Frohnapfel, and J. Kriegseis. Formation and decay of vorticity in impulsively stopped infinite cylinders. *16th European Turbulence Conference - ETC16 , Stockholm, Sweden*, 2017.

[9] LEGI. Matlab toolbox uvmat, 2017. URL http://servforge.legi.grenoble-inp.fr/projects/soft-uvmat.

[10] LEGI - UMR 5519. Coriolis rotating platform, 2017. URL http://www.legi.grenoble-inp.fr/web/spip.php?article757.

[11] D. M. Mathis and G. P. Neitzel. Experiments on impulsive spin-down to rest. *The Physics of fluids*, 28(2): 449–454, 1985.

[12] G. P. Neitzel and S. H. Davis. Centrifugal instabilities during spin-down to rest in finite cylinders. numerical experiments. *Journal of Fluid Mechanics*, 102:329–352, 1981.

[13] F. Nordsiek, S. G. Huisman, R. C. A. van der Veen, C. Sun, D. Lohse, and D. P. Lathrop. Azimuthal velocity profiles in rayleigh-stable taylor–couette flow and implied axial angular momentum transport. *Journal of Fluid Mechanics*, 774:342–362, 2015.

[14] James O'Donnell and P.F. Linden. Free-surface effects on the spin-up of fluid in a rotating cylinder. *J. Fluid Mech.*, 232:439–453, 1991.

[15] PIVTEC GmbH. *User Manual*. URL http://www.pivtec.com/download/docs/PIVview_v24_Manual.pdf.

[16] L. Rayleigh. On the dynamics of revolving fluids. *Proceedings of the Royal Society of London*, 93(648): 148–154, 1917.